metals

MDPI

Article

Unraveling Copper Nucleation from Cu(I) in Reline: Coupling Thermodynamics, Kinetics and Interfacial Structure

Beatriz Maldonado-Teodocio [1], Manuel Palomar-Pardavé [1], Mario Romero-Romo [1], Claudia Ramírez [2], Perla Morales-Gil [3], Miguel Torres-Rodríguez [4] and María G. Montes de Oca-Yemha [1,*]

[1] Departamento de Materiales, Universidad Autónoma Metropolitana-Azcapotzalco, Av. San Pablo 420, Col. Nueva El Rosario, Alcaldía Azcapotzalco, Mexico City 02128, Mexico; beatriz.mal.teo@gmail.com (B.M.-T.); mepp@azc.uam.mx (M.P.-P.); mmrr@azc.uam.mx (M.R.-R.)
[2] Departamento de Ingeniería en Metalurgia y Materiales, Instituto Politécnico Nacional, ESIQIE, Mexico City 07738, Mexico; cramirezro@ipn.mx
[3] Laboratorio de Caracterización de Materiales Sintéticos y Naturales, Instituto Mexicano del Petróleo, Eje Central Lázaro Cárdenas 152, Mexico City 07730, Mexico; moralesp@imp.mx
[4] Departamento de Ciencias Básicas, Universidad Autónoma Metropolitana-Azcapotzalco, Av. San Pablo 420, Col. Nueva El Rosario, Alcaldía Azcapotzalco, Mexico City 02128, Mexico; trm@azc.uam.mx
* Correspondence: mgmy@azc.uam.mx

Abstract

The nucleation and growth mechanisms of copper electrodeposition from Cu(I)-containing-reline, a deep eutectic solvent, were investigated through a combination of electrochemical techniques and surface characterization. Cyclic voltammetry revealed the characteristic nucleation loop associated with an overpotential-driven electrocrystallization process, from which the equilibrium potential of the Cu(I)/Cu(0) redox couple was determined to be −0.35 V vs. a Ag quasi-reference electrode. Experimental potentiostatic current density transients were analyzed using nucleation models capable of accounting for both adsorption and three-dimensional (3D) diffusion-controlled growth, thereby allowing deconvolution of the individual contributions to the overall current response. The kinetic parameters, including the nucleation frequency and the number density of active sites, exhibited an exponential dependence on the applied overpotential, thus indicating enhanced nucleation kinetics at greater driving forces, while determining a Cu(I) diffusion coefficient of $(3.39 + 0.09) \times 10^{-7}$ cm^2 s^{-1}. Thermodynamic analysis showed that the Gibbs free energy of the formation of the critical nucleus decreases with increasing overpotential and follows the expected dependence on the inverse square of the overpotential, in agreement with classical nucleation theory. The estimated critical nucleus size was found to be smaller than one atom, suggesting that nucleation occurs at highly active surface sites. Furthermore, an exchange current density of (3 ± 1) μA cm^{-2} was estimated for the Cu(I) electrochemical reduction. Scanning electron microscopy revealed a high density of copper nanoparticles (~20 nm) distributed across the electrode surface, along with larger aggregates (~100 nm) formed by coalescence and growth, consistent with a progressive nucleation mechanism. X-ray photoelectron spectroscopy confirmed that the deposits consist exclusively of metallic copper, with no evidence of oxidized species. These results demonstrate that copper electrodeposition in reline is governed by a complex interplay between the thermodynamic driving force, the interfacial kinetics, and mass transport, comprehensively providing fundamental insight into the electrocrystallization processes in deep eutectic solvents.

Keywords: copper electrodeposition; deep eutectic solvent (reline); electrochemical nucleation and growth; potentiostatic current transients

Check for updates

Academic Editor: Nebojša Nikolić

Received: 1 May 2026
Revised: 10 June 2026
Accepted: 12 June 2026
Published: 16 June 2026

Copyright: © 2026 by the authors. Licensee MDPI, Basel, Switzerland. This article is an open access article distributed under the terms and conditions of the Creative Commons Attribution (CC BY) license.

1. Introduction

The electrochemical nucleation and growth of metals are fundamental processes that determine the microstructure, morphology, and functional properties of electrodeposited films. Among metallic systems, copper nanoparticles remain one of the most technologically relevant materials due to their widespread applications in catalysis [1], electrocatalysis [2], removal of pollutants from wastewater samples [3], biocatalyst and bioremediation [3], and antimicrobial applications [4]. Notedly, achieving precise control over copper film morphology requires a rigorous understanding of the thermodynamic driving forces and kinetic pathways governing electrocrystallization, particularly during the earliest stages of nucleation and growth.

In recent years, deep eutectic solvents (DESs) have emerged as promising alternatives to conventional aqueous electrolytes for metal electrodeposition [5–14]. Their negligible vapor pressure, wide electrochemical window, high ionic strength, and ability to stabilize reactive metal species make them attractive media for fundamental electrochemical studies. In particular, reline, a eutectic mixture of choline chloride and urea in a 1:2 molar ratio, [5,9–11,14] forms a hydrogen-bonded network that significantly modifies ion solvation, activity coefficients, and interfacial properties compared with aqueous systems.

Within this structured ionic environment, the electrochemical behavior of copper species differs substantially from that observed in water-based electrolytes. While copper is commonly deposited from Cu(II) precursors in aqueous media [15–19], the use of Cu(I) salts introduces a mechanistically different system [19]. In these aqueous solutions, Cu(I) is thermodynamically unstable and undergoes disproportionation (2Cu(I) → Cu(II) + Cu(0)) [20]. However, as shown in the pioneer works of Nila and Gonzalez [21], see Figures 1 and 7 in Reference [21], and Montes de Oca et al. [22], see Figure 1 in Reference [22], in aqueous media and depending on both chloride concentration and pH, Cu(I) can be stabilized as chlorocuprate complexes, suppressing such disproportionation. A very similar situation occurs in chloride-rich DESs such as ethaline [6,7] and reline [9,10]. However, copper electrochemical deposition becomes more complex since the following faradaic reactions can be simultaneously present, depending on the applied potential considered [9,10]:

$$\mathrm{Cu(II)_{Reline}} + \mathrm{e^-} \rightarrow \mathrm{Cu(I)_{Reline}} \quad (1)$$

$$\mathrm{Cu(I)_{Reline}} + \mathrm{e^-} \underset{b}{\overset{f}{\rightleftharpoons}} \mathrm{Cu(0)} \quad (2)$$

$$\mathrm{Cu(II)_{Reline}} + 2\mathrm{e^-} \rightarrow \mathrm{Cu(0)} \quad (3)$$

Consequently, undertaking a study on Cu electrodeposition from its Cu(I) precursor is justified from both thermodynamic and kinetic perspectives. Thermodynamically, the formal potential of the Cu(I)/Cu(0) system in reline is strongly influenced by complexation equilibria and solvent–ion interactions. These factors alter the effective overpotential required for reduction and directly impact the Gibbs free energy barrier for nucleation (ΔG*). Since the nucleation rate depends exponentially on overpotential, even modest shifts in redox potential or interfacial energy significantly modify the critical nucleus size and nucleation density [23].

Kinetically, the Cu(I) → Cu(0) process involves a single-electron transfer, see reaction 1, eliminating the sequential reduction steps characteristic of Cu(II) systems. This simplification allows a clearer interpretation of charge-transfer mechanisms and facilitates the elucidation of intrinsic kinetic parameters, including standard rate constants, transfer coefficients, and the Cu(I) diffusion coefficient. For this purpose, chronoamperometric

transients can be recorded and analyzed [11], thereby providing a deeper insight into the electrocrystallization dynamics in structured ionic media.

Importantly, stabilization of Cu(I) species in reline enables copper deposition at potentially smaller overpotentials while minimizing parasitic reactions such as hydrogen evolution. This not only enhances mechanistic clarity but also supports the development of controlled nanostructured copper films with tunable grain size and morphology.

Therefore, investigating the thermodynamic parameters (formal potential, interfacial free energy, and nucleation energy barrier) together with kinetic descriptors (electron-transfer rate constants, diffusion coefficients, nucleation rate, and growth mechanism) of copper electrodeposition from Cu(I) precursors dissolved in reline provide both fundamental and technological value. Such studies duly advance electrocrystallization theory in DES and contribute to designing sustainable, precisely controlled copper deposition strategies in emerging green electrolyte systems.

2. Materials and Methods

2.1. Reactants and Reline DES Preparation

The reactants used were choline chloride (ChCl, Sigma-Aldrich, 99%) (St. Louis, MO, USA), urea (U, Sigma-Aldrich, 99%) (St. Louis, MO, USA), copper chloride (CuCl, Merck, 99%) (Schnelldorf, Germany) and deionized water (18.2 MΩ cm).

Reline DES was obtained by mixing choline chloride and urea in a 1:2 molar ratio under stirring at 50 °C on a heating plate. After, the CuCl was added as the precursor salt at 5 mM to a volume of 50 mL, continuously stirring the mix for an additional 24 h at a fixed 50 °C. The resulting solution containing Cu(I) in reline DES was termed Cu(I)–reline, while the eutectic mixture without the precursor salt was called blank.

2.2. Electrochemical Studies

Copper nanoparticle formation onto the glassy carbon electrode (GCE) surface was studied by potentiodynamic and potentiostatic techniques using a conventional three-electrode glass cell that comprised the Cu(I)–reline, a silver wire as the quasi-reference electrode (Ag QRE), a platinum wire as the counter electrode, and a GCE as the working electrode. Before electrodeposition, the surface area of the GCE (0.1963 cm^2) was polished with 1.0 and 0.3 μm alumina. Cyclic voltammetry (CV) and chronoamperometry (CA) techniques were conducted in triplicate at 70 °C, as this temperature ensures low viscosity and high electrical conductivity of the DES. These experiments were performed using an Admiral potentiostat-galvanostat Squidstat Plus, manufactured by Admiral Instruments (Tempe, AZ, USA), coupled to a PC running the Squidstat User Interface (SUI) software v2.06.15.2023 for experimental control and data acquisition.

2.3. Characterization of Electrodeposits

The characterization of the Cu electrodeposits was performed using SEM-SEI to determine the Cu morphology onto the GCE, and a section analysis of some of these SEM images was performed using Gwyddion 2.66 software and EDS to confirm the elemental composition of the electrodeposits, using a JEOL, 7000 JSM-6701F scanning electron microscope (JEOL Ltd., Akishima, Tokyo, Japan) equipped with an Oxford EDS detector (OXINST, High Wycombe, UK) at 15 kV. Furthermore, to determine the chemical state of the intervening elements, studies were carried out with X-ray photoelectron spectroscopy (XPS) with K-alfa Thermo Fisher Equipment (base pressure 2×10^{-9} mbar, West Sussex, UK) with an Al filament emitting X-rays at 1489 eV.

3. Results and Discussion

3.1. Potentiodynamic Study

Figure 1a compares the cyclic voltammograms (CVs) recorded with a GCE immersed in pure reline (blank) and in reline containing Cu(I) ions. In the absence of Cu(I), the voltammogram exhibits the typical response associated with capacitive processes occurring in the electrical double layer formed at the GCE/reline interface [24]. In contrast, when Cu(I) ions are present, a cathodic peak (cp) appears during the forward (f) potential scan together with a corresponding anodic peak (ap) during the backward (b) scan. These peaks are attributed to the faradaic reaction 2.

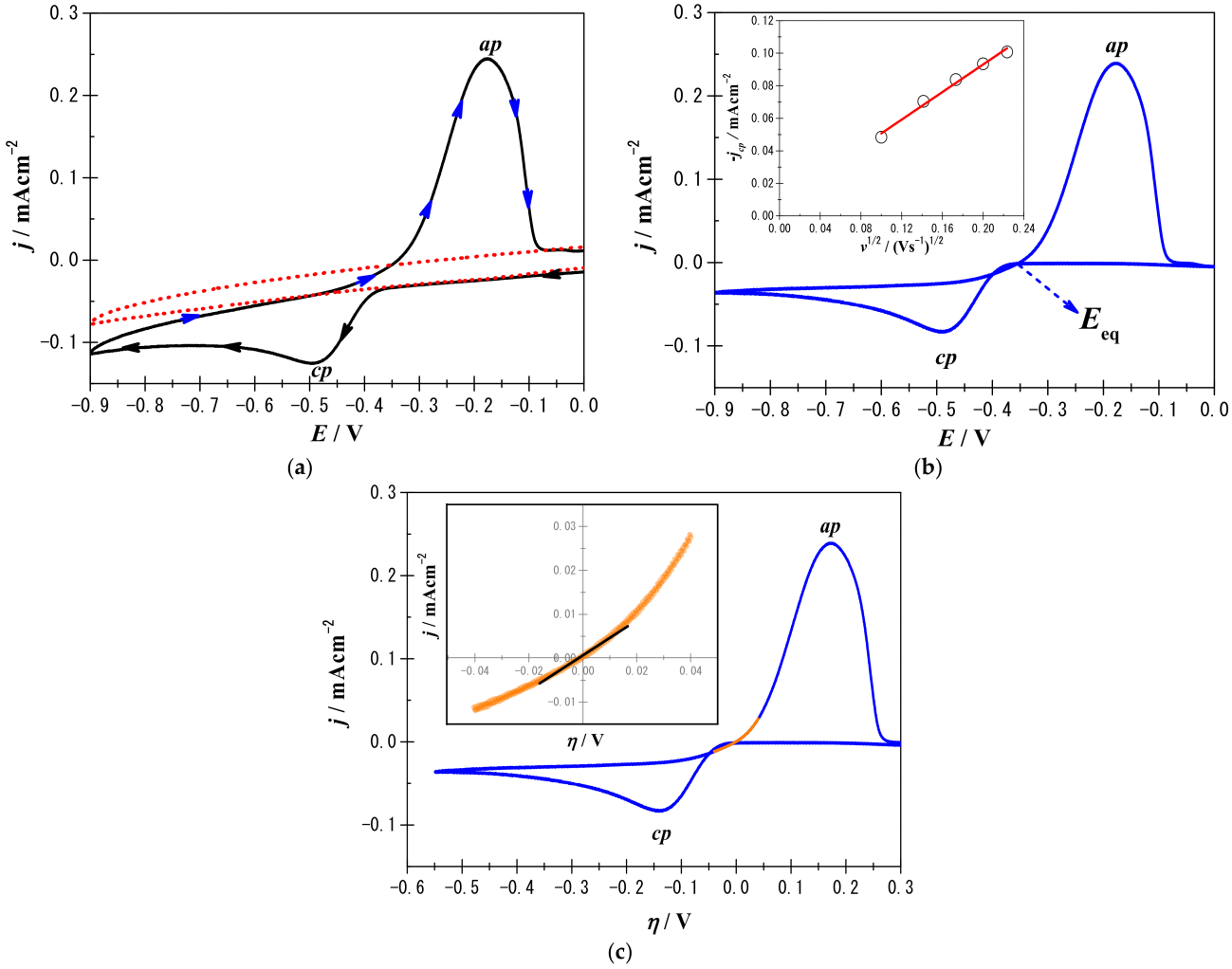


Figure 1. (**a**) Comparison of cyclic voltammograms (CVs) recorded for the systems GCE/reline in the absence (blank, dotted red trace) and in the presence of 5 mM Cu(I) (solid black line), at a scan rate of 30 mV s^{-1} and 70 °C. In both cases, the potential scan started at 0 mV in the negative direction. (**b**) CV obtained after background subtraction (blank). The inset depicts the variation in the cathodic peak current density (j_{cp}) as a function of the potential scan rate (points), together with the corresponding linear fit. (**c**) CV obtained after subtracting the E_{eq} value from all applied potentials in the CV shown in (**b**). The inset displays a section of the anodic branch around zero overpotential, including the experimental data (orange points) and the corresponding fitting equation analyzed using the low-field approximation of the Butler–Volmer equation (Equation (4)), black line.

After subtracting the response of the GCE/reline without the precursor, the blank, from that of the GCE/reline 5 mM Cu(I), the CV in Figure 1b is obtained, which depicts the net electrochemical response of the system containing Cu(I). The characteristic loop

formed by the forward (cathodic) and backward (anodic) potential scans becomes clearly distinguishable. This loop is associated with a nucleation process that requires the activation energy provided by overpotential and is characterized by a higher cathodic current density during the reverse scan than during the forward scan [25].

The potential at which the current density returns to zero after this loop, approximately −0.35 V in this case, provides an estimate of the equilibrium potential (E_{eq}) of the Cu(I)/Cu(0) redox couple. At E_{eq}, the forward and backward current densities (j_f and j_b), respectively, are equal (see reaction 2). However, when the overpotential ($\eta = E - E_{eq}$) differs from zero, a net current flows through the electrode, as illustrated in Figure 1c.

The inset of Figure 1c shows the j–η plot constructed from the experimental data obtained during the reverse sweep of the cyclic voltammogram in the potential region close to E_{eq}. Therein, the current density varies linearly with the overpotential. Therefore, the data were analyzed using the small overpotential approximation of the Butler–Volmer equation (valid for small η values), as expressed in Equation (4). The fitting equation used is also shown in Figure 1c. From this analysis, the exchange current density (j_0) for reaction 2 was determined to be (3 ± 1) μA cm^{-2}.

Moreover, as the inset of Figure 1b shows, the cathodic peak current density (j_{cp}) exhibits a linear dependence on the square root of the potential scan rate, indicating that under these overpotential conditions the copper nucleation is a diffusion-controlled process, as established by the well-known Berzins–Delahay equation (see Equation (1) in Reference [11]).

$$j = \frac{j_0 z F}{RT}\eta \tag{4}$$

where j is the current density, F is the Faraday constant, R is the universal gas constant, T is the temperature, z is the number of electrons transferred, and η is the overpotential.

3.2. Potentiostatic Study

Figure 2a shows a comparison of experimental potentiostatic current density transients (j–t) recorded at the same applied overpotential in pure reline (blank) and in reline containing Cu(I) ions. After subtraction of the blank response, the transient shown in Figure 2b was obtained. The same procedure was applied for the other overpotentials, see Table 1, considered in this work, and the resulting transients are presented in Figure 2c.

Table 1. Best-fit parameters obtained from the nonlinear fitting of Equation (16) to the experimental j–t transients shown in Figure 2c.

$-\eta$ /V	k_1 /mAcm^{-2}	k_2 /s^{-1}	P_1 /mAcm^{-2} s$^{-1/2}$	P_2 /s^{-1}	P_3 /s^{-1}
0.27	0.09 ± 0.01	10.1 ± 0.2	0.160 ± 0.001	1.0 ± 0.1	5.1 ± 0.2
0.29	0.11 ± 0.01	11.1 ± 0.2	0.160 ± 0.001	1.2 ± 0.2	6.4 ± 0.2
0.31	0.12 ± 0.01	13.1 ± 0.2	0.161 ± 0.001	1.6 ± 0.1	8.5 ± 0.2
0.33	0.16 ± 0.01	16.6 ± 0.3	0.161 ± 0.001	2.1 ± 0.2	9.6 ± 0.2
0.35	0.17 ± 0.01	17.7 ± 0.3	0.159 ± 0.002	2.8 ± 0.3	10.2 ± 0.1
0.37	0.18 ± 0.02	18.6 ± 0.2	0.157 ± 0.004	3.6 ± 0.2	11.6 ± 0.1
0.39	0.18 ± 0.02	22.1 ± 0.1	0.156 ± 0.004	4.4 ± 0.1	14.6 ± 0.1
0.41	0.18 ± 0.01	26.5 ± 0.1	0.158 ± 0.003	5.8 ± 0.3	19.7 ± 0.1
0.43	0.17 ± 0.01	35.8 ± 0.2	0.155 ± 0.004	6.7 ± 0.3	25.3 ± 0.2
0.45	0.17 ± 0.01	40.7 ± 0.2	0.157 ± 0.004	8.5 ± 0.2	27.1 ± 0.2

Figure 2c shows the experimental current density transients (j–t) that exhibited an abrupt decay of the current density seen within the very early stages, which is associated with adsorption phenomena. Subsequently, the plot follows the typical three dimensional (3D) nucleation and growth profile [26], where the current density rising trend attains a

maximum after which the transient decays with increasing time. Such behavior was reported previously for copper overpotential deposition on Au(111) [15] and silver deposition on GCE [27], both from aqueous solutions. At different overpotentials, it is known that while the absolute value of the current density maximum (j_m) increases, its corresponding time (t_m) diminishes. This behavior follows the Scharifker and Hills (SH) model [26], which describes two limiting cases for three-dimensional nucleation under diffusion control: instantaneous and progressive nucleation.

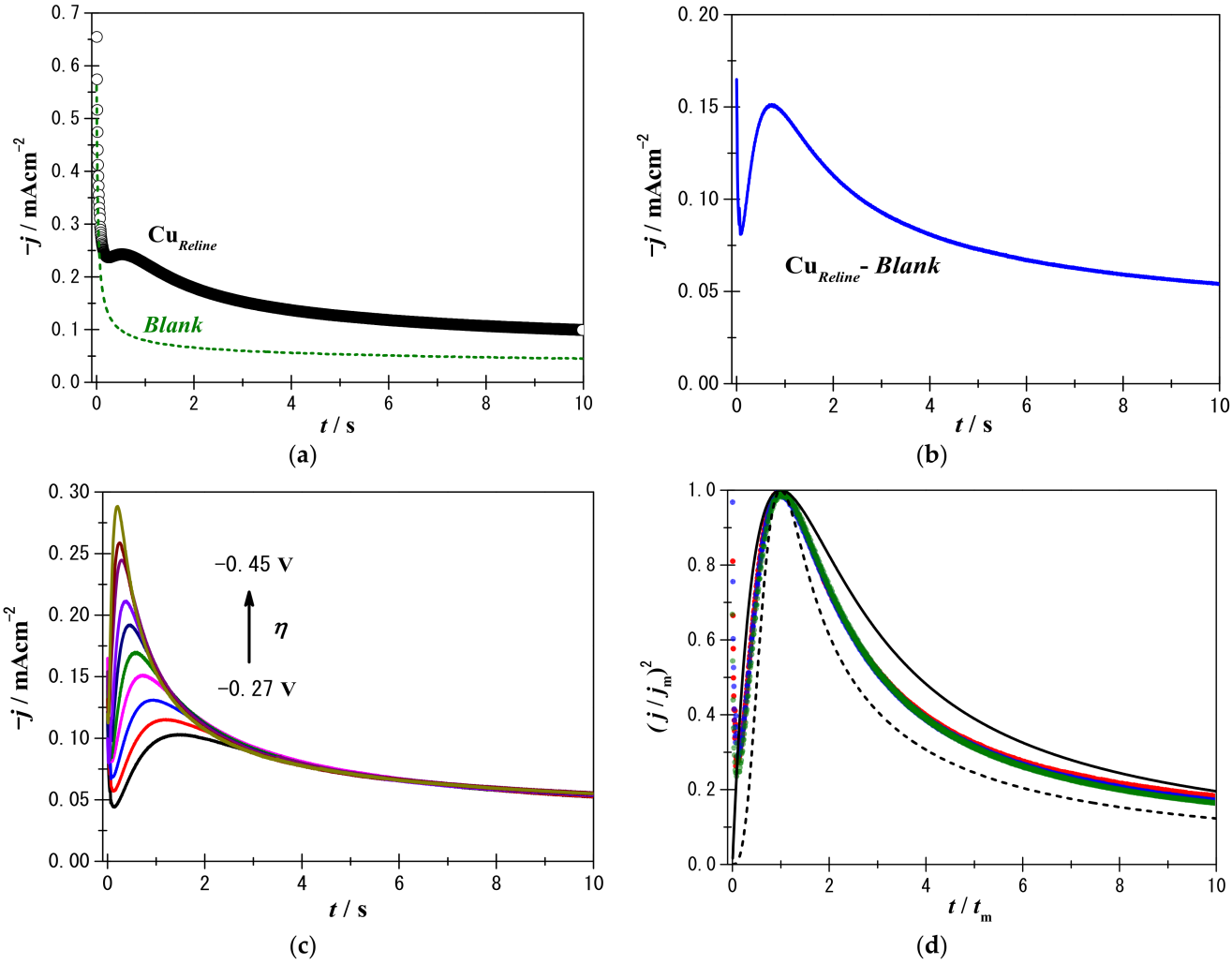


Figure 2. (**a**) Comparison of experimental current density transients recorded in the GCE/reline system in the absence (blank, broken line) and in the presence of 5 mM Cu(I) (open circles) at an overpotential of $\eta = -0.33$ V. (**b**) Example of current density–time transient obtained after subtraction of (**a**). (**c**) Family of *j*–*t* transients recorded at different overpotential values (in V) after subtraction of the corresponding blank responses. (**d**) Comparison of selected normalized transients from panel (**c**), obtained at = $\eta = -0.31$ V (red), $\eta = -0.33$ V (blue), and $\eta = -0.35$ V (green). The experimental plots were normalized using their corresponding maximum current density, j_m, and time values, t_m, and compared with the theoretical models for three-dimensional nucleation under diffusion control: instantaneous nucleation (solid line) and progressive nucleation (broken line).

Figure 2d compares the dimensionless current density transients obtained at −0.31, −0.33 and −0.35 V with instantaneous or progressive nucleation and growth. In this case, the dimensionless transients do not comply with the limiting cases proposed by the SH model [26]. That being the case, a more complex model for an adequate description of the process is needed.

The analysis was carried out to assume the total density current results of the superposition of two contributions (Equation (5)). For the 3D nucleation contribution, $j_{3D}(t)$, the Heerman–Tarallo (HT) model [28] was employed by the parameterized equation (Equation (6)), in which the Dawson integral is approximated by a polynomial expression (see Equation (10)), following the approach reported by Arbib et al. [29]. For the adsorption contribution, $j_{ads}(t)$, Equation (7) was used, as proposed by Hölzle et al. [30] to describe adsorption and double-layer charging processes.

$$j_{total}(t) = j_{ad}(t) + j_{3D}(t) \tag{5}$$

with

$$j_{3D}(t) = P_1 t^{-1/2} \frac{\Phi}{\varphi} \theta(t) \tag{6}$$

$$j_{\text{ads}}(t) = k_1 \exp(-k_2 t) \tag{7}$$

where

$$\theta(t) = (1 - \exp(-P_2 t \varphi(t))) \tag{8}$$

$$\varphi(t) = 1 - \frac{1 - \exp(-At)}{At} \tag{9}$$

$$\Phi(t) = 1 - \frac{\exp(-At)}{(At)^{\frac{1}{2}}} \int_0^{(\mathrm{At})^{\frac{1}{2}}} \exp\left(\lambda^2\right) d\lambda \cong 1 - \left[\frac{a + b\,(At)^{\frac{1}{2}}}{\left(1 - c\,(At)^{\frac{1}{2}} + d * At\right)(At)^{\frac{1}{2}}} \right] \tag{10}$$

$$P_1 = \frac{zFD^{1/2}C_0}{\pi^{1/2}} \tag{11}$$

$$P_2 = (2\pi)^{3/2} D (MC_0/\rho)^{1/2} N_0 \tag{12}$$

$$k_1 = \frac{E}{R_s} \tag{13}$$

$$k_2 = \frac{1}{R_s C} \tag{14}$$

$$Q_{\text{ads}} = \frac{k_1}{k_2} \tag{15}$$

Therefore, Equation (5) can be parameterized as follows:

$$j(t) = k_1 \exp(-k_2 t) + P_1 t^{-1/2} \left(\frac{1 - \left[\frac{a + b\,(At)^{\frac{1}{2}}}{\left(1 - c\,(At)^{\frac{1}{2}} + d * At\right)(At)^{\frac{1}{2}}} \right]}{1 - \frac{1 - \exp(-At)}{\mathrm{At}}} \right) \left(1 - \exp\left(-P_2 t \left(1 - \frac{1 - \exp(-At)}{\mathrm{At}} \right) \right) \right) \tag{16}$$

In these equations, λ is the integration variable, C_0 and D are the bulk concentration and diffusion coefficient of Cu(I), respectively, M and ρ are the atomic mass and density of Cu, respectively, and z is the number of electrons transferred during Cu nucleation. F is the Faraday constant; A is the copper deposit nucleation frequency and N_0 is the number density of active sites for copper nucleation on the electrode surface. The numerical values a = 0.051314213, b = 0.47910725, c = 1.2068142 and d = 1.185724 correspond to the parameters of a polynomial approximation to the Dawson integral. R_s is the solution's resistance, C the double layer capacitance and Q_{ads} is the charge density of the adsorption process.

Figure 3a shows a comparison between one of the experimental j–t transients presented in Figure 2c and the corresponding theoretical curve obtained by nonlinear fitting of

Equation (16) to the experimental data. It can be observed that the theoretical model accurately describes the entire transient.

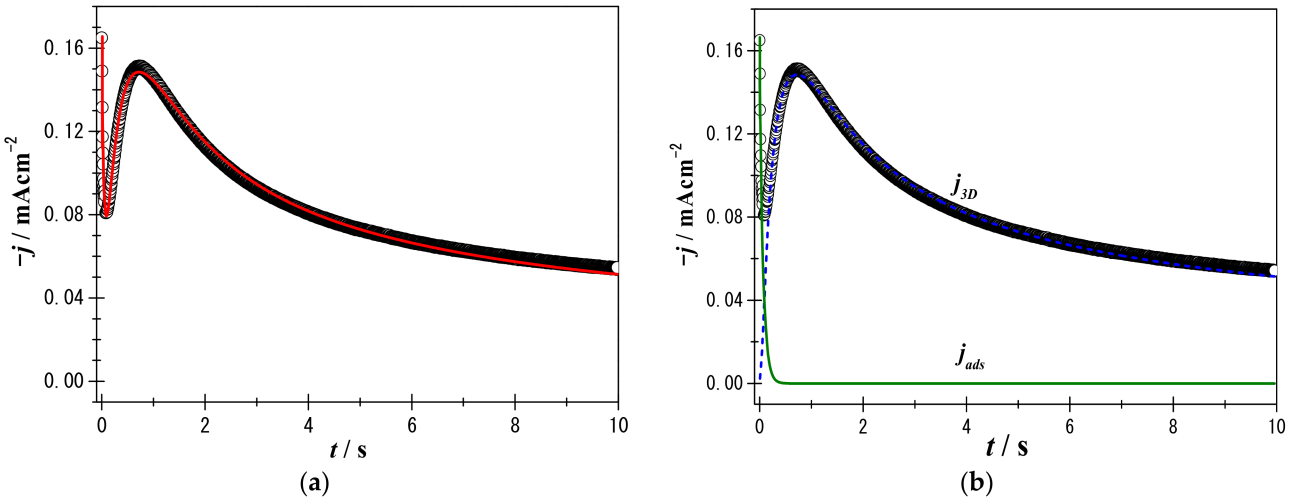


Figure 3. (**a**) Comparison of the *j*–*t* plot depicted in Figure 2c recorded at $\eta = -0.33$ V (open circles) with the theoretical one (red line) obtained after nonlinear fitting of the experimental values with the model depicted in Equation (16). (**b**) Individual contributions to the overall current density defined in Equation (16), calculated from Equation (3) for the 3D nucleation term, $j_{3D}(t)$, and Equation (4) for the adsorption term, $j_{ads}(t)$, using the best-fit parameters listed in Table 1.

Furthermore, note that at the very early stages the adsorption process, $j_{ads}(t)$, is the dominant contribution, as shown in Figure 3b; however, it rapidly decreases to zero, while the contribution of 3D nucleation, $j_{3D}(t)$, becomes predominant over most of the transient. The model employed in this work enables the deconvolution of these two contributions.

The best-fit parameters obtained from this analysis are summarized in Table 1.

Using the best-fit parameters reported in Table 1, the kinetic parameters associated with the nucleation and growth mechanism during the early stages of Cu electrodeposition were determined (see Table 2). The values of the nucleation frequency, A, and number density of active sites, N_0, increase exponentially through the application of more negative overpotentials, as shown in Figures 4a and 4b, respectively.

Table 2. Kinetic parameters calculated from the non-linear fitting of Equation (16) to the experimental *j*–*t* transients shown in Figure 2c.

$-\eta$ /V	A /s^{-1}	$10^{-8}\ N_0$ [1] /cm^{-2}	$10^{7}\ D$ [2] /cm^2 s^{-1}
0.27	5.1 ± 0.2	0.31 ± 0.03	3.45 ± 0.01
0.29	6.4 ± 0.2	0.38 ± 0.02	3.47 ± 0.01
0.31	8.5 ± 0.2	0.49 ± 0.02	3.49 ± 0.01
0.33	9.6 ± 0.2	0.64 ± 0.01	3.51 ± 0.01
0.35	10.2 ± 0.1	0.86 ± 0.01	3.41 ± 0.02
0.37	11.6 ± 0.1	1.17 ± 0.01	3.33 ± 0.04
0.39	14.6 ± 0.1	1.44 ± 0.01	3.29 ± 0.04
0.41	19.7 ± 0.1	1.83 ± 0.01	3.39 ± 0.03
0.43	25.3 ± 0.2	2.20 ± 0.01	3.26 ± 0.04
0.45	27.1 ± 0.2	2.73 ± 0.01	3.33 ± 0.04

Estimated from [1] Equation (12) and [2] Equation (11), using the corresponding parameters reported in Table 1.

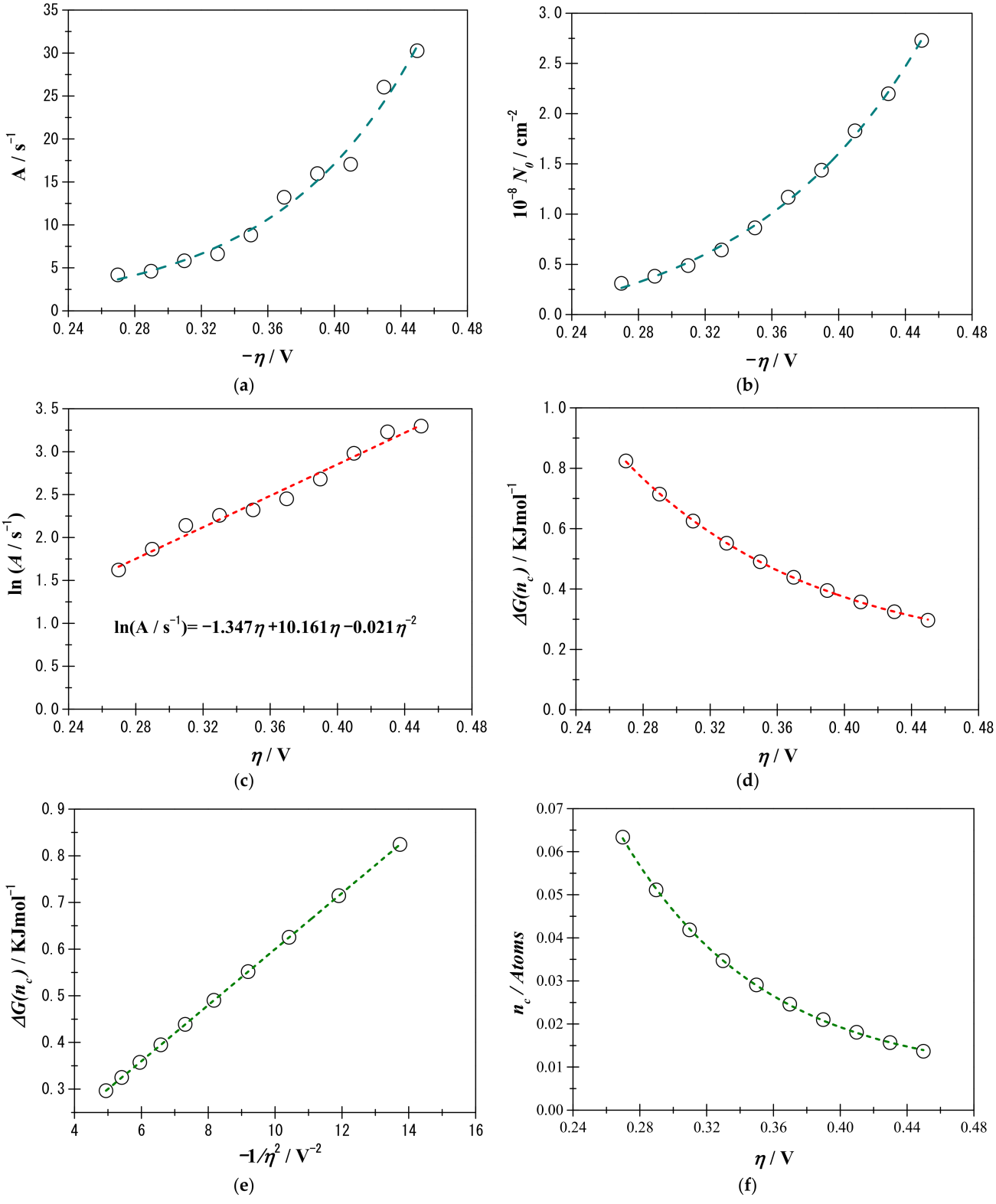


Figure 4. Overpotential dependence of (**a**) the nucleation frequency and (**b**) the number density of active sites, obtained from the analysis of the experimental current density transients shown in Figure 2c (see also Table 2). In both cases, the broken lines correspond to exponential fits of the experimental data. (**c**) Resulting relationship from the nonlinear fitting of Equation (17) to the nucleation frequency as a function of overpotential. Variation in the Gibbs free energy of formation of the critical nucleus, $\Delta G(n_c)$ (markers), determined from the analysis of the ln A vs. η plot (see panel (**c**)) using Equation (17), plotted as a function of η (**d**) and $1/\eta^2$ (**e**). (**f**) Critical nucleus size as a function of the applied overpotential, calculated using Equation (22).

An average diffusion coefficient for Cu(I) of $(3.39 \pm 0.09) \times 10^{-7}$ cm^2 s^{-1} was estimated. This value is in good agreement with that reported by Sebastián et al. [9] for Cu(I) in reline at a 50 mM concentration, namely 3.2×10^{-7} cm^2 s^{-1}.

Furthermore, the dependence of the nucleation frequency on the applied overpotential (Figure 4c) provides valuable insight into the thermodynamic and kinetic aspects governing the nucleation process of new phases. By fitting Equation (17) to the experimental data, key parameters were extracted, including the Gibbs free energy of formation of the critical nucleus, $\Delta G(n_c)$, the number of atoms in the critical nucleus, n_c, the exchange current density, j_0, the charge-transfer coefficient, α, and the interfacial surface tension, σ, at the electrode/deposit/electrolyte interface, following the methodology described in [31]. These parameters are summarized in Table 3. Notably, the j_0 value is consistent with that obtained independently from the potentiodynamic study, as described above.

Table 3. Kinetic and thermodynamic parameters resulting from fitting Equation (17) to the ln (A) vs. η (see Figure 4c) obtained from analysis of the experimental j–t plots reported in Figure 2c.

α [1]	j_0 [2] /mA cm^{-2}	$10^5\sigma$ [3] /J cm^{-2}	n_c [4]
0.3 ± 0.1	4.7± 0.4	1.3 ± 0.2	<1

Estimated using: [1] (Equation (19)), [2] (Equation (18)), [3] (Equation (20)) and [4] (Equation (22)).

The exponential increase in nucleation frequency with increasing overpotential reflects the progressive reduction in the nucleation energy barrier, which enhances the probability of forming stable nuclei and accelerates the overall nucleation rate. Accordingly, the decrease in $\Delta G(n_c)$ with increasing driving force, see Figure 4d, is consistent with the simultaneous increase in Cu nucleation frequency and active site density discussed above, confirming that Cu nucleation is strongly activated under these conditions.

In the context of reline, these trends can be further understood considering the unique physicochemical properties of DESs. The relatively high viscosity and the presence of strong hydrogen-bonding networks between choline chloride and the hydrogen bond donor led to reduced ionic mobility and enhanced ion–ion interactions. In particular, Cu(I) species are known to form stable complexes within the DES environment, which can hinder mass transport and modify the effective electrochemical activity of the metal precursor. As a result, higher overpotentials are required to overcome both kinetic and transport limitations, leading to a more pronounced dependence of nucleation parameters on the applied potential.

Moreover, the interfacial structure of DESs, characterized by specific adsorption and structured solvent layers at the electrode surface, may influence the effective surface tension σ and the critical nucleus size. This structured environment can facilitate the stabilization of small clusters at sufficiently negative overpotentials, thereby promoting a transition toward faster nucleation kinetics and diffusion-controlled three-dimensional growth. Overall, these results highlight the interplay between thermodynamic driving force, interfacial structure, and transport properties in governing the early stages of copper electrodeposition in reline.

$$\ln(A) = K_1 + K_2\eta - K_3\eta^{-2} \tag{17}$$

with

$$K_1 = ln\left(\frac{\sqrt{2}v_a j_0 \sigma^{1/2}}{z(kT)^{1/2}e}\right) \tag{18}$$

$$K_2 = \frac{z\alpha e}{kT} \tag{19}$$

$$K_3 = -\frac{8\pi\sigma^3 v_a^2}{3(ze)^2 kT} \quad (20)$$

where k is the Boltzmann constant, e is the elemental charge and v_a is the atomic volume.

The nucleation work is defined as the difference between the Gibbs free energy of an aggregate containing n atoms in the new phase (formed on the electrode surface) and that of the same number of metal ions in solution [32]. This quantity depends on the degree of supersaturation, which, in electrochemical systems, is governed by the applied overpotential. The nucleation work reaches a maximum at the critical nucleus size, n_c, and the corresponding free energy of nucleation, $\Delta G(n_c)$, is therefore an overpotential-dependent parameter, as described by Equation (21).

Figure 4 illustrates the variation in $\Delta G(n_c)$ as a function of η (Figure 4d) and $1/\eta^2$ (Figure 4e). As the overpotential increases, $\Delta G(n_c)$ decreases significantly, reflecting the progressive reduction in the nucleation energy barrier and, consequently, a more favorable nucleation process at higher driving forces. This trend is fully consistent with classical nucleation theory and is further supported by the linear dependence of $\Delta G(n_c)$ on $1/\eta^2$, which agrees well with the prediction of η (21).

This thermodynamic behavior is directly correlated with the kinetic parameters obtained in this work. In particular, the exponential increase in both the nucleation frequency, A, and the number density of active sites, N_0, with increasing overpotential can be rationalized by the reduction in $\Delta G(n_c)$. As the nucleation barrier decreases, a larger fraction of surface sites becomes energetically favorable for nucleation, leading to a higher density of active nuclei and a faster overall nucleation rate. Similarly, the value of the exchange current density, j_0, reflects the enhanced charge-transfer kinetics under these conditions, further facilitating the transition from ion reduction to stable nucleus formation.

Remarkably, the estimated critical nucleus size is smaller than one atom (Figure 4f), suggesting that nucleation occurs at highly active surface sites where the formation of a stable nucleus requires minimal atomic aggregation. This result is consistent with the interpretation proposed by Milchev [32], in which a single active site on the electrode surface can effectively act as a critical nucleus. Such behavior may be indicative of a highly heterogeneous surface, where specific sites—such as defects, edges, or functional groups on the glassy carbon electrode—serve as preferential nucleation centers.

In the context of reline, these effects are likely amplified by the unique physicochemical properties of DESs. The high viscosity and the presence of an extended hydrogen-bonding network can limit mass transport while promoting strong interactions between Cu(I) species and the solvent environment. Additionally, the formation of stable Cu(I) complexes and the structured interfacial layers at the electrode surface can modify both the effective surface energy and the local supersaturation conditions. As a result, higher overpotentials are required to overcome these constraints, leading to a pronounced coupling between thermodynamic driving force and kinetic response. Overall, these findings demonstrate that copper nucleation in reline is governed by a subtly intricate interplay between interfacial energetics, charge-transfer kinetics, and transport limitations, which collectively control the early stages of electrodeposition.

$$\Delta G(n_c) = \frac{8\pi\sigma^3 v_a^2}{3(ze)^2\eta^2} = -\frac{kTK_3}{\eta^2} \quad (21)$$

$$n_c = \frac{2\Delta G(n_c)}{ze\eta} \quad (22)$$

3.3. SEM, EDS and XPS Characterization

Figure 5 shows SEM images recorded at different magnifications after potentiostatic copper electrodeposition, together with the corresponding EDS spectrum. The images formed through collecting secondary electrons emitted by the sample conform to the low-magnification images presented, where diverse copper nanoparticles, CuNPs, appear randomly distributed over an area of the GCE (see Figure 5a,b).

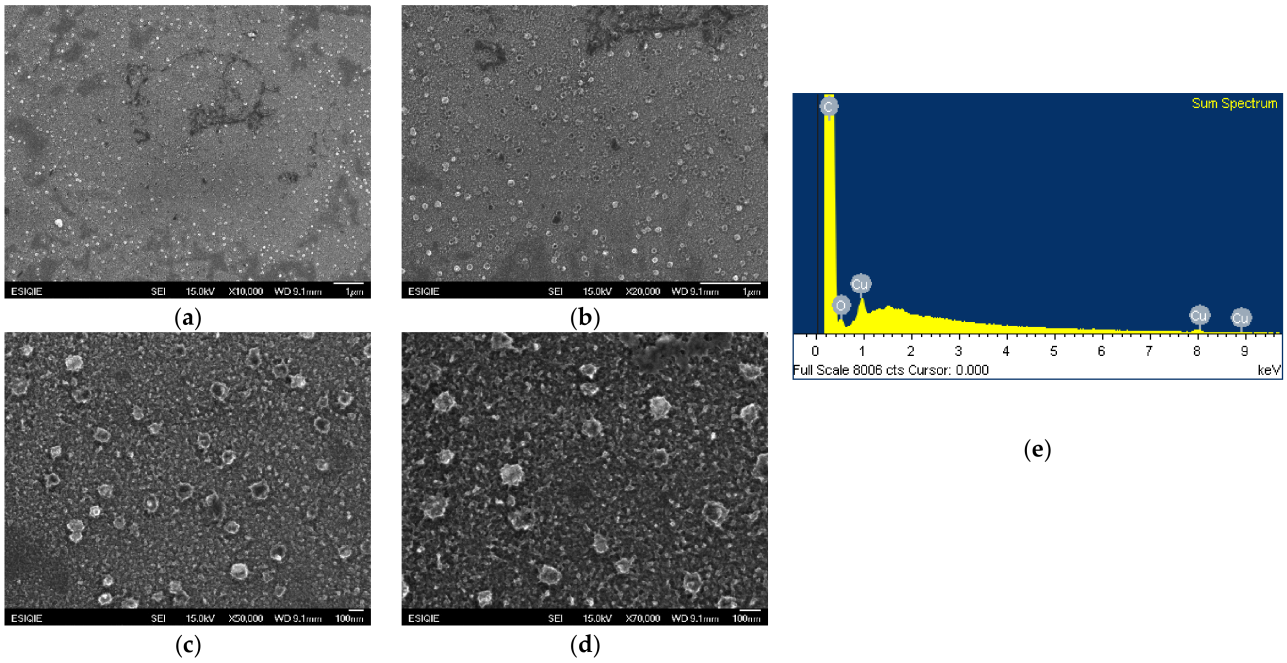
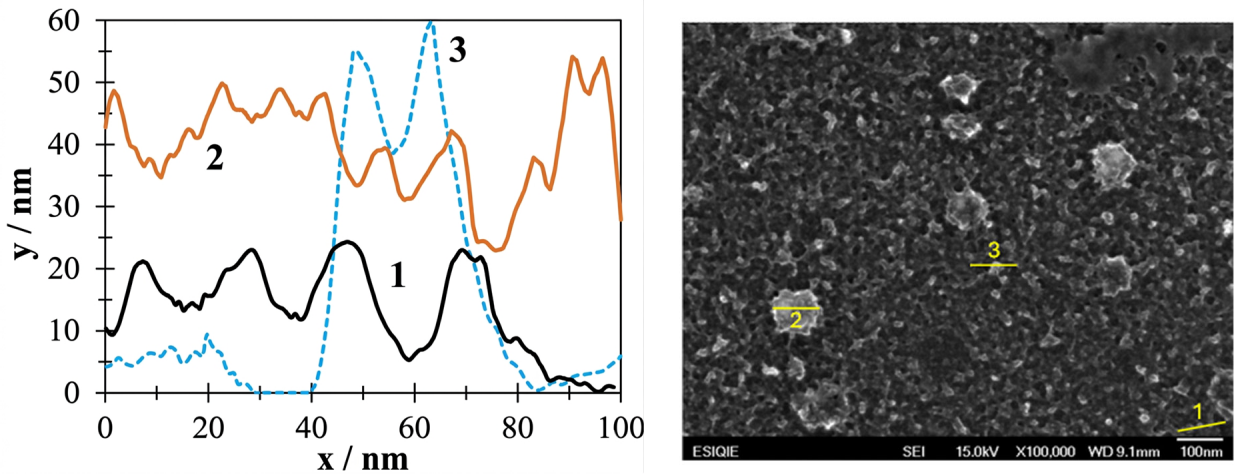


Figure 5. SEM images recorded at different magnifications of (**a**) 10,000×, (**b**) 20,000×, (**c**) 50,000× and (**d**) 70,000× of the GCE surface after potentiostatic copper electrodeposition at $\eta = -0.33$ V (see Figure 3a,b) and (**e**) the corresponding EDS spectrum.

When comparing the nanocrystals photographed in Figure 5c,d, the irregular overall aspect of the CuNPs becomes apparent. The objects depicted have different scales and shapes, which strongly suggest different growth intervals. The CuNPs grew differently, although their initial growths have long since passed through the scale of the critical nuclei size. Figure 5d shows that the CuNPs have evolved in size and adopted diverse growing directions that puts them in the category of appreciable 3D aggregates. Figure 5e was produced through collecting the X-ray photon emission of the element present in the deposit, clearly showing the presence of Cu.

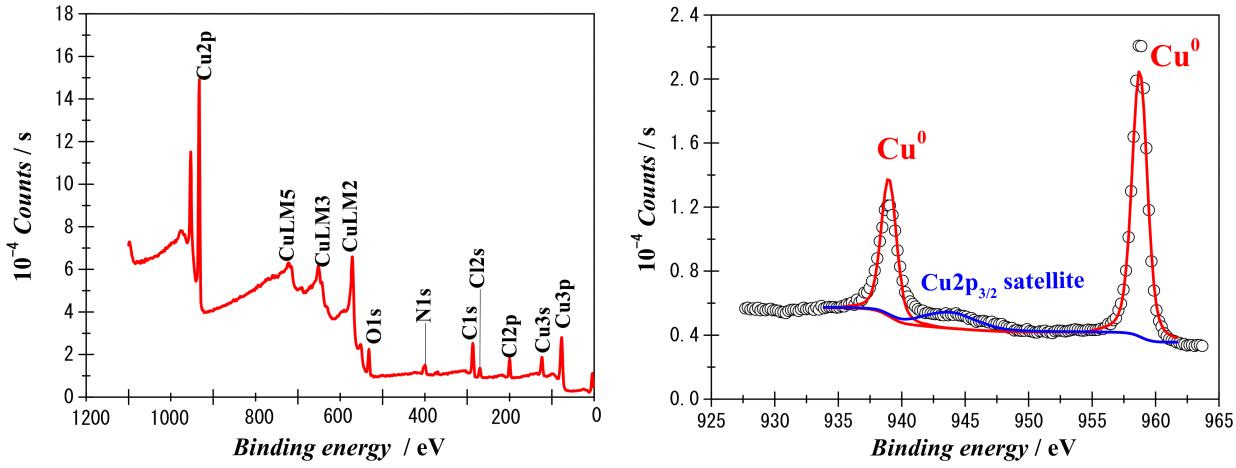
Figure 6a shows a topographic line profile from an SEM image, see Figure 6b, that notably shows an aggregate with a dimension of approximately 100 nm, referred to as axis "x" (see line 2 in Figure 6a). The aggregate appears brighter due to its larger size and height. It becomes apparent that the deposit comprises an appreciable majority of smaller nuclei with sizes of the order of ~20 nm (see line 1 in Figure 6a), which exhibit lower height profiles. These smaller nanoparticles act as the fundamental building units that progressively coalesce to form larger aggregates, reaching heights of up to ~50 nm, referred to as the "y" axis (see profile 2 in Figure 6a). A limited number of wider aggregates with comparable heights can be identified (see line 3 in Figure 6a), suggesting some degree of lateral growth and coalescence.



(**a**) (**b**)

Figure 6. (**a**) Line profiles traced over the directions indicated in the SEM image shown in panel (**b**). (**b**) SEM image recorded at a magnification of 100,000× used for the line profile analysis.

This morphological evolution is consistent with the nucleation and growth mechanism inferred from the electrochemical analysis. The high density of small nuclei supports a scenario of progressive nucleation, in which new nuclei continue to form over time rather than a simultaneous all-nucleating occurrence. As deposition proceeds, diffusion-controlled three-dimensional (3D) growth dominates, leading to the enlargement and eventual coalescence of neighboring nuclei into larger aggregates. The coexistence of small nuclei and larger clusters reflects the dynamic balance between nucleation and growth processes, in agreement with the kinetic parameters and transient analysis discussed above. Furthermore, the XPS results (Figure 7), including both the survey spectrum and the high-resolution Cu 2p region, confirm that these nuclei are composed exclusively of metallic copper. In particular, the absence of shake-up satellite peaks and the characteristic binding energy position of the Cu $2p_3/_2$ signal are consistent with Cu^0, indicating that no significant amounts of Cu(I) or Cu(II) species are present on the electrode surface. This finding confirms that the electrodeposition process leads to the direct formation of metallic copper under the studied conditions.



(**a**) (**b**)

Figure 7. (**a**) Survey XPS spectrum recorded on the surface shown in Figure 6b. (**b**) Comparison between the experimental high-resolution XPS spectrum of the Cu 2p region (open circles) and the fitted curve (red line), corresponding to metallic copper. The blue line represents a higher satellite binding energy characteristic peak of Cu(II).

4. Conclusions

The outcomes from the present manuscript have managed to unravel a truly important interrelation among three basically important aspects dealt with in metal electrodeposition, namely the overpotential, the nucleation, the growth kinetics and the morphology of the deposit obtained. This endeavor constitutes a valuable novel mechanistic proposition on the copper electrodeposition from DES reline. To validate this relationship, a detailed analysis of the electrochemical transients was carried out, providing quantitative insights into the underlying nucleation and growth processes.

The analysis of *j–t* transients using appropriate nucleation models allowed the separation of adsorption and nucleation contributions, demonstrating that adsorption dominates at very short times, whereas 3D nucleation and growth govern the overall deposition process. The nucleation parameters, including the nucleation frequency (A) and the number density of active sites (N_0), exhibited an exponential increase with increasing overpotential, reflecting the strong influence of the applied driving force on the nucleation kinetics.

The evidence garnered that sums up the electrochemical evidence, namely that of thermodynamics in the morphology analysis, leads us to conclude that copper electrodeposition from a Cu(I)-containing reline followed a diffusion-controlled 3D nucleation and growth mechanism. This is supported by the basic fact that the increasing overpotential favored exponential increases in the nucleation frequency and the density of active sites while at the same reducing the Gibbs free energy difference associated with formation of the critical nuclei. SEM morphology evidence directly ascertained the kinetic foresights derived from chronoamperometry, whereas XPS analyses affirmed the formation of metal copper devoid of other chemical species over the surface of the nanocrystals formed.

Author Contributions: Conceptualization, B.M.-T., M.P.-P. and M.G.M.d.O.-Y.; methodology, B.M.-T., M.R.-R., C.R. and P.M.-G.; software, M.P.-P.; validation, B.M.-T., C.R. and P.M.-G.; formal analysis, B.M.-T., M.R.-R., M.T.-R., M.G.M.d.O.-Y. and M.P.-P.; investigation, B.M.-T., M.R.-R., C.R. and P.M.-G.; resources, M.G.M.d.O.-Y. and M.P.-P.; data curation, B.M.-T., M.G.M.d.O.-Y. and M.P.-P.; writing—original draft preparation, B.M.-T., M.G.M.d.O.-Y., M.R.-R. and M.P.-P.; writing—review and editing, B.M.-T., M.G.M.d.O.-Y., M.R.-R., P.M.-G. and M.P.-P.; visualization, C.R. and M.T.-R.; supervision, M.P.-P. and M.G.M.d.O.-Y.; project administration, M.P.-P.; funding acquisition, M.G.M.d.O.-Y. and M.P.-P. All authors have read and agreed to the published version of the manuscript.

Funding: This research was funded by Universidad Autónoma Metropolitana.

Data Availability Statement: The data presented in this study are available on request from the corresponding author.

Acknowledgments: B.M.T. gratefully acknowledges the financial support provided by the Secretariat of Science, Humanities, Technology and Innovation (SECIHTI) to pursue postgraduate studies at Universidad Autónoma Metropolitana–Azcapotzalco. M.G.M.Y., M.R.R., P.M.G., M.T.R. and M.P.P. thank the SNII for the distinction of their membership and the stipend received. The authors would like to thank the project "Cuerpos de agua en el Estado de México: monitoreo de contaminantes y una propuesta para su eliminación basada en tratamientos biológicos y de oxidación avanzada", granted within the interinstitutional (UAMEX-IPN-UAM) collaboration framework.

Conflicts of Interest: The authors declare no conflicts of interest.

References

1. Pathak, R.; Punetha, V.D.; Bhatt, S.; Punetha, M. A review on copper-based nanoparticles as a catalyst: Synthesis and applications in coupling reactions. *J. Mater. Sci.* **2024**, *59*, 6169–6205. [CrossRef]
2. Farid, S. A brief review of oxide-derived materials for selective electrochemical reduction of CO_2. *Discov. Electrochem.* **2026**, *3*, 7. [CrossRef]

3. Bhagat, M.; Anand, R.; Sharman, P.; Rajput, P.; Sharman, N.; Sing, K. Review—Multifunctional Copper Nanoparticles: Synthesis and Applications. *ECS J. Solid State Sci. Technol.* **2021**, *10*, 063011. [CrossRef]
4. Crisan, M.C.; Teodora, M.; Lucian, M. Copper Nanoparticles: Synthesis and Characterization, Physiology, Toxicity and Antimicrobial Applications. *Appl. Sci.* **2022**, *12*, 141. [CrossRef]
5. Abbott, A.P.; El Ttaib, K.; Frisch, G.; McKenzie, K.J.; Ryder, K.S. Electrodeposition of copper composites from deep eutectic solvents based on choline chloride. *Phys. Chem. Chem. Phys.* **2009**, *11*, 4269–4277. [CrossRef] [PubMed]
6. Vukmirovic, M.B.; Adzic, R.R.; Akolkar, R. Copper Electrodeposition from Deep Eutectic Solvents. Voltammetric Studies Providing Insights into the Role of Substrate: Platinum vs Glassy Carbon. *J. Phys. Chem. B* **2020**, *124*, 5465–5475. [CrossRef] [PubMed]
7. Fu, X.; Zhan, C.; Zhang, R.; Wang, B.; Sun, H.; Sun, J. Effect of temperature on mechanism and kinetics of electrochemical nucleation of copper in ChCl-based deep eutectic solvents. *J. Solid State Electrochem.* **2022**, *26*, 2713–2722. [CrossRef]
8. Tan, Z.; Liu, S.; Wu, J.; Nan, Z.; Yang, F.; Zhan, D.; Yan, J.; Mao, B. Copper Deposition on Au(111) in a Deep Eutectic Solvent: An In Situ STM Study. *ChemElectroChem.* **2022**, *9*, e202101412. [CrossRef]
9. Sebastián, P.; Vallés, E.; Gómez, E. Copper electrodeposition in a deep eutectic solvent. First stages analysis considering Cu (I) stabilization in chloride media. *Electrochim. Acta* **2014**, *123*, 285–295. [CrossRef]
10. Sebastián, P.; Vallés, E.T.E.; Molina, A.; Gómez, E. Advances in copper electrodeposition in chloride excess. A theoretical and experimental approach. *Electrochim. Acta* **2015**, *164*, 187–195. [CrossRef]
11. Hernández-Pérez, D.; Aldana-González, J.; Romero-Romo, M.; Rivera-Hernández, S.; Ezeta-Mejía, A.; Morales-Gil, P.; Sánchez-Piñón, N.; Sampayo-Garrido, A.; Palomar-Pardavé, M. Electrochemical Nucleation and Growth of Neodymium Electrodes using Reline as a Deep Eutectic Solven. *Electrochim. Acta* **2025**, *535*, 146643. [CrossRef]
12. Escobar-Monsalvo, N.; Aldana-González, J.; Romero-Romo, M.; Gil, P.M.; López-Medina, R.; Ramírez-Silva, M.T.; Guzmán-Hernández, D.S.; Le, M.T.; Palomar-Pardavé, M. Cadmium Electrodeposition on Glassy Carbon from Ethaline Deep. Eutectic Solvent: Electrochemical and Surface Analysis. *J. Electrochem. Soc.* **2025**, *172*, 092514. [CrossRef]
13. Mejía-Caballero, I.; Manh, T.L.; Aldana-González, J.; Arce-Estrada, E.M.; Romero-Romo, M.; Campos-Silva, I.; Ramírez-Silva, M.T.; Palomar-Pardavé, M. Electrodeposition of nanostructured chromium conglomerates from Cr(III) dissolved in a deep eutectic solvent: Influence of forced convection. *J. Electrochem. Soc.* **2021**, *168*, 112512. [CrossRef]
14. Juárez-Marmolejo, L.; Maldonado-Teodocio, B.; De Oca-Yemha, M.G.M.; Romero-Romo, M.; Arce-Estrada, E.M.; Ezeta-Mejía, A.; Ramírez-Silva, M.T.; Mostany, J.; Palomar-Pardavé, M. Electrocatalytic oxidation of formic acid by palladium nanoparticles electrochemically synthesized from a deep eutectic solvent. *Catal. Today* **2022**, *394–396*, 190–197. [CrossRef]
15. Pardavé, M.P.; González, I.; Batina, N. New Insights into Evaluation of Kinetic Parameters for Potentiostatic Metal Deposition with Underpotential and Overpotential Deposition Processes. *J. Phys. Chem. B* **2000**, *104*, 3545–3555. [CrossRef]
16. Palomar-Pardavé, M.; Garfias-García, E.; Romero-Romo, M.; Ramírez-Silva, M.T.; Batina, N. Influence of the substrate's surface structure on the mechanism and kinetics of the electrochemical UPD formation of a copper monolayer on gold. *Electrochim. Acta* **2011**, *56*, 10083. [CrossRef]
17. Aldana-González, J.; Olvera-García, J.; De Oca, M.G.M.; Romero-Romo, M.; Ramírez-Silva, M.T.; Palomar-Pardavé, M. Electrochemical quantification of the electro-active surface area of Au nanoparticles supported onto an ITO electrode by means of Cu upd. *Electrochem. Commun.* **2015**, *56*, 70–74. [CrossRef]
18. Romero-Romo, M.; Aldana-González, J.; Botello, L.E.; De Oca, M.G.M.; Ramírez-Silva, M.T.; Corona-Avendaño, S.; Palomar-Pardavé, M. Electrochemical nucleation and growth of Cu onto Au nanoparticles supported on a Si (111) wafer electrode. *J. Electroanal. Chem.* **2017**, *791*, 1–7. [CrossRef]
19. Milchev, A.; Zapryanova, T. Nucleation and growth of copper under combined charge transfer and diffusion limitations: Part I. *Electrochim. Acta* **2006**, *51*, 2926–2933. [CrossRef]
20. Lewandowski, A. Ionic solvation. Part 4—Copper (I) solvation. Disproportionation and halide-complex formation in propylene carbonate. *J. Chem. Soc. Faraday Trans. 1* **1988**, *84*, 4013–4021. [CrossRef]
21. Nila, C.; González, I. The role of pH and Cu(II) concentration in the electrodeposition of Cu(II) in NH4Cl solutions. *J. Electroanal. Chem.* **1996**, *401*, 171–182. [CrossRef]
22. Yemha, M.G.M.d.O.; Mostany, J.; Ramírez-Silva, M.T.; Romero-Romo, M.; Scharifker, B.R.; Palomar-Pardavé, M. Electrodeposition Under Forced Convection Conditions. *ECS Trans.* **2007**, *3*, 117–125. [CrossRef]
23. Lin, J.; Kilani, M.; Baharfar, M.M.; Wang, R.R.; Mao, G. Understanding the nanoscale phenomena of nucleation and crystal growth in electrodeposition. *Nanoscale* **2024**, *16*, 19564–19588. [CrossRef] [PubMed]
24. Abbott, A.P.; Barron, J.C.; Frisch, G.; Gurman, S.; Ryder, K.S.; Silva, A.F. Double layer effects on metal nucleation in deep eutectic solvents. *Phys. Chem. Chem. Phys.* **2011**, *13*, 10224–10231. [CrossRef] [PubMed]
25. Palomar-Pardavé, M.; Ramírez-Silva, M.T.; Aldana-González, J.; Botello, L.E.; Arce-Estrada, E.M.; Mostany, J.; Romero-Romo, M. Influences of temperature on the thermodynamics and kinetics of cobalt electrochemical nucleation and growth. *Electrochim. Acta* **2017**, *241*, 162–169. [CrossRef]

26. Scharifker, B.; Hills, G. Theoretical and experimental studies of multiple nucleation. *Electrochim. Acta* **1983**, *28*, 879–889. [CrossRef]
27. Ramírez, C.; Arce, E.M.; Romero-Romo, M.; Palomar-Pardavé, M. The effect of temperature on the kinetics and mechanism of silver electrodeposition. *Solid State Ion.* **2004**, *169*, 81–85. [CrossRef]
28. Heerman, L.; Tarallo, A. Theory of the chronoamperometric transient for electrochemical nucleation with diffusion-controlled growth. *J. Electroanal. Chem.* **1999**, *470*, 70–76. [CrossRef]
29. Arbib, M.; Zhang, B.; Lazarov, V.; Stoychev, D.; Milchev, A.; Buess-Herman, C. Electrochemical nucleation and growth of rhodium on gold substrates. *J. Electroanal. Chem.* **2001**, *510*, 67–77. [CrossRef]
30. Hölzle, M.H.; Retter, U.; Kolb, D.M. The kinetics of structural changes in Cu adlayers on Au(111). *J. Electroanal. Chem.* **1994**, *371*, 101–109. [CrossRef]
31. Sebastián, P.; Botello, L.E.; Vallés, E.; Gómez, E.; Palomar-Pardavé, M.; Scharifker, B.R.; Mostany, J. Three-dimensional nu-cleation with diffusion controlled growth: A comparative study of electrochemical phase formation from aqueous and deep eutectic solvents. *J. Electroanal. Chem.* **2017**, *793*, 119–125. [CrossRef]
32. Milchev, A. *Electrocrystallization: Fundamentals of Nucleation and Growth*; Kluwer Academic Publishers: Boston, CA, USA, 2002.

Disclaimer/Publisher's Note: The statements, opinions and data contained in all publications are solely those of the individual author(s) and contributor(s) and not of MDPI and/or the editor(s). MDPI and/or the editor(s) disclaim responsibility for any injury to people or property resulting from any ideas, methods, instructions or products referred to in the content.